Figure S1. PAF Expression in Lung Cancer, Related to Figure 1.

(A) Transcriptional upregulation of *PAF* in human cancer. Oncomine analysis of *PAF* expression in human cancer. The numbers in parentheses represent the total number of analyzed data sets between normal versus indicated cancers. *PAF* expression is highly upregulated in lung cancer (15 of 37 analyses, 40.54%; gene rank > top 10%, fold change > 2; *P*-value < 0.0001; compared to normal tissues).

(B) Kaplan–Meier (KM) survival curves for non-small cell lung cancer (NSCLC), lung adenocarcinoma (LUAD), and lung squamous cell carcinoma (LUSC) by *PAF* expression (different probe [202503_s_at] for cDNA microarrays). Data sets including 1926 NSCLC, 720 LUAD, and 524 LUSC patients were analyzed using the publicly available tool KM plotter.

(C) KM survival curves for 504 LUAD and 495 LUSC patients based on *PAF* expression. (KM plotter; RNA-Seq ID: PCLAF).

(D) KM survival curves for 488 LUSC patients in the TCGA database by *PAF* expression. The lowest quartile was used as the cutoff for dividing PAF-low and PAF-high groups (GEPIA; TCGA).

(E and F) Transcript variants of PAF. (E) The *PAF* (*PCLAF/KIAA0101*) gene is transcribed into two variants, variant 1 (*Var. 1*) and variant 2 (*Var. 2*). PAF *Var. 1* includes a conserved PCNA-interacting motif (PIP-motif: 62Q-69F) (Emanuele et al., 2011). Two ubiquitination modification residues in PAF are located at lysines 15 (K15) and 24 (K24), which is essential for PCNA interaction in S phase (Povlsen et al., 2012). (F) Expression of transcript variants of *PAF*. *PAF Var. 1* showed higher expression in two LUAD cell lines (A549, H1792); qRT-PCR.

(G) Expression of Paf in $Kras^{LSL\text{-}G12D/+}$ lung tumors. Co-immunostaining of Paf and Pcna in lung tumors of $Kras^{LSL\text{-}G12D/+}$ mice (4 mo after Ad-Cre induction); scale bars = 20 μm.

Figure S2. Suppression of Lung Tumorigenesis by *Paf* KO, Related to Figure 2.

(A and B) Paf expression in proliferating mouse lung tumor cells. Black-and-white images of Figures 2A and 2B. Co-immunostaining of (A) Paf/Ki67 and (B) Paf/Pcna in KP mouse lung tumors; scale bars = 50 μm.

(C and D) Suppression of lung tumorigenesis by *Paf* KO. (C) Micro-CT analysis of lungs from KP and PKP mice. KP (3 mo after Ad-Cre injection, n = 6) and PKP (3 mo; tumor undetected: n = 4, detected: n = 2, and 8 mo; n = 3) mice were analyzed. Scale bars = 2 mm; H: heart; asterisk: tumor lesion. (D) Representative H&E staining images of PKP lungs at the endpoint of observation (dead at 11 mo; n = 1); scale bars = 2 mm for whole lung sections and 100 μm for magnified images of tumors.

(E) Decreased cell proliferation on *Paf* KO background. Representative Ki67 staining of KP and PKP lung tumors; scale bars = 50 μm.

(F and G) No impact of *Paf* KO on cell death. (F) Immunofluorescent (IF) staining of cleaved caspase-3 in KP and PKP lung tumors. Scale bars = 50 μm. (G) Quantification of cleaved caspase-3 staining of KP and PKP lung tumors. At least 15 fields of 200× magnified images from KP (n = 4), and PKP (n = 9) lung tumors were analyzed; error bars: SD; n.s.: not significant.

(H) H&E staining images of lungs from *Paf*$^{-/-}$; *Kras*$^{LSL\text{-}G12D/+}$ (PK) mice at 22 months after Ad-Cre induction; scale bar = 2 mm for whole lung sections and 100 μm for magnified images of tumors.

(I) *Paf* KO reduced cell proliferation in *Kras*$^{G12D/+}$-driven lung tumors. Ki67 staining of *Kras*$^{LSL\text{-}G12D/+}$ (K) and *Paf*$^{-/-}$; *Kras*$^{LSL\text{-}G12D/+}$ (PK) lung tumors; scale bars = 50 μm.

(J and K) No effect of *Paf* KO on apoptosis of *Kras*$^{G12D/+}$-driven lung tumors. (J) Cleaved caspase-3 staining of K and PK lung tumors; scale bar = 50 μm. (K) Quantification of cleaved caspase-3 staining of K and PK lung tumors. More than 15 fields of 200× magnified images from K (n = 4) and PK (n = 5) lung tumors were analyzed; n.s.: not significant.

(L and M) No effects of *Paf* KO on Cre-loxP recombination in *Kras*$^{LSL\text{-}G12D/+}$ and *Paf*$^{-/-}$; *Kras*$^{LSL\text{-}G12D/+}$ lungs. (L) Staining of Kras^{G12D} with anti- Ras^{G12D} antibody in K and PK lungs 10 days after Ad5-CMV-Cre infection (1×10^9 PFU); scale bar = 50 μm. (M) Quantification of Kras^{G12D}-expressing cells near the bronchiole region of K and PK lungs. More than 10 fields of 200× magnified images from K (n = 3) and PK (n = 3) lungs were analyzed; n.s.: not significant.

Representative images are shown.

Figure S3. PAF Depletion Induced Cell Quiescence and Growth Arrest in Lung Cancer Cells, Related to Figure 3.

(A) The establishment and validation of mouse KP lung cancer cell lines. Three mouse lung cancer cell lines were established from lung tumors from three independent KP mice (mouse ID numbers KP836, KP952, and KP944). Recombinant alleles of *Kras*^{G12D} and deletion of *Trp53* were confirmed by genomic DNA PCR. *Kras* WT: 622 bp, *Kras*$^{LSL\text{-}G12D}$: 500 bp, recombinant *Kras*^{G12D}: 650 bp, WT *Trp53*: 288 bp, *Trp53*$^{floxed/floxed}$: 370 bp, *Trp53*$^{\Delta/\Delta}$: 612 bp.

(B) Bright-field and fluorescent (GFP) images of KP mouse lung cancer cells infected with control shRNA (pLenti-shGPF) and two Paf-knockdown shRNAs (pLenti-shPaf-GFP; #1 and #2). Scale bars = 50 μm.

(C-F) IB analysis of PAF knockdown by shPAFs in mouse and human LUAD cell lines. Depletion of endogenous Paf by shPafs (#1 and #2) in KP cells, confirmed by IB of stably transduced KP cells (C) and its rescue by ectopic PAF expression (D). IB analysis of PAF knockdown by shPAFs in human A549 LUAD cells (E) and its rescue by ectopic PAF expression (F).

(G) PAF rescue experiment of PAF-depleted human A549 LUAD cells. Cumulative population doublings of cells stably expressing shRNAs or PAF. Two-way ANOVA with Tukey *post hoc* test.

(H and I) No increased cell death by PAF depletion. (H) Immunohistochemistry (IHC) analysis of cleaved caspase-3 (CC3) in control (shCtrl) versus PAF KD (shPAF) lung cancer cells (A549 and H1792). (I) Quantification of CC3-positive cells in control versus PAF KD lung cancer cells; error bars: SEM. Scale bars = 20 μm.

(J) Quantification of cell cycle phases in KP and human lung cancer cells (control and Paf KD) in Figures 3F and 3G. PI staining with FACS analysis.

(K) Monitoring of G0/G1 cell cycle arrest using a DHB-Venus reporter system in control (shCtrl) versus PAF KD (shPAF) H1792 lung cancer cells. Each cell (marked with a number) was monitored for 24 h. shCtrl cells (labeled with 1 and 2) showing nuclear DHB-Venus at 0 h underwent release from the G0/G1 phase at 24 h. However, PAF-depleted cells exhibited G0/G1 arrest (indicated by nuclear localization of DHB-Venus) at 0 and 24 h. Scale bars = 50 μm.

(L and M) PAF-PCNA binding is not required for PAF depletion-induced cell quiescence and growth arrest. (L) PAF mutPIP rescues PAF-depletion induced cell growth arrest. Cumulative population doublings of cells stably expressing shRNAs with GFP or PAF mutPIP. Two-way ANOVA with Tukey *post hoc* test. (M) Ectopic expression of PCNA-binding deficient PAF mutants (FLAG epitope-tagged PAF^{K15R}, PAF^{K24R}, or PAF$^{K15R/K24R}$) rescues PAF depletion-induced growth inhibition in A549 cells; cumulative population doublings. Two-way ANOVA with Tukey *post hoc* test.

Representative images are shown; error bars: SEM; *P < 0.05; **P < 0.01.

Figure S4. Correlated Expression of PAF and DREAM Complex Targets in Lung Adenocarcinoma, Related to Figure 4.

(A) Hierarchically clustered heatmap of common differentially expressed genes (DEGs) (n = 122) in control versus PAF-depleted mouse (KP) and human lung cancer (H1792) cells. DEGs were analyzed by RNA-Seq. Mean values are shown (n = 2).

(B) Heatmaps showing comparative analyses of the expression of *PAF* and PAF-DREAM target genes in the Oncomine data sets (normal lungs and lung adenocarcinomas); *PAF* (*KIAA0101*) and 19 representative PAF-DREAM targets were analyzed; each horizontal row represents an individual patient sample, and the vertical boxes represent the relative expression level of the indicated gene. Of note, PAF is barely expressed in normal lung samples. Three representative data sets are shown, (Landi Lung [normal tissue = 49, LUAD = 58], Selamat Lung [normal tissue = 56, LUAD = 58], and Okayama Lung [normal tissue = 20, LUAD = 226]); heatmaps show $\log_2$ median-centered intensity.

Figure S5. DREAM Complex Mediates PAF Depletion-Induced Cell Quiescence and Growth Arrest of Lung Cancer Cells, Related to Figure 5.

(A and B) Treatment with harmine, an inhibitor of DYRK1A, rescues the G0/G1 arrest of PAF-depleted KP and LUAD (A549 and H1792) cells. The cell cycle distribution of each cell line was analyzed by PI staining and FACS. (A) Cell cycle distribution of harmine-treated control (shCtrl) and PAF KD (shPaf) KP cells and (B) quantification.

(C) Cell cycle distribution of harmine-treated control (shCtrl) A549 and H1792 cells.

(D) Harmine treatment rescued G0/G1 arrest caused by PAF depletion with shPAF#1 in A549 and H1792 cells, as with shPAF #2 (see Figure 5A and 5B).

(E) Harmine treatment reduced the G0/G1 arrest induced by PAF KD in three other lung cancer cell lines (H23, H358, and H1355); Cell cycle phases in indicated conditions were analyzed by PI staining and FACS; Represent images of at least two times experiments (n>2). Similar rescue responses were observed.

(F and G) Depletion of DYRK1A rescues the G0/G1 arrest induced by PAF depletion. The density scatter plot shows cell cycle phases in shDYRK1A-GFP–transfected PAF KD H1792 cells (H1792 shPAF). (G) The cell cycle phases were analyzed in GFP-positive (sh-DYRK1A-GFP with shPAF) and GFP-negative (shPAF) cells by 7-AAD staining with FACS. (G) Quantification of cell cycle phases.

Representative images are shown; error bars: SEM; $*P < 0.05$; $**P < 0.01$.

Figure S6. Analysis of the Interaction between PAF and RBBP4/DREAM Complex, Related to Figure 6.

(A and B) Interaction of PAF with RBBP4. A549 cells were transfected with indicated plasmids and analyzed by co-IP and IB. Interaction of endogenous RBBP4 with FLAG-PAF (upper panel); Binding of endogenous PAF to FLAG-RBBP4 (lower panel). (B) Endogenous interaction between Paf and Rbbp4 in KP cells. Paf-IP (upper panel) and Rbbp4-IP (lower panel). Two different anti-PAF antibodies (ab56773 and G-11) were used for co-IP-IB (upper panel). Immunoglobulin G (IgG): negative control for IP. PAF is shown as doublet-bands, consistent with the previous studies (Povlsen et al., 2012).

(C-F) Interaction of PAF with DREAM complex components. (C) A549 and KP cells stably expressing FLAG-PAF were used for co-IP and IB analyses. Co-IP showed that FLAG-PAF interacts with LIN9 and LIN54 but not with p130-E2F4 and FOXM1. (D-F) Endogenous interaction between PAF and DREAM complex components. Co-IP detected that endogenous PAF interacts with LIN54 and BMYB (D and E). IP using PAF antibody detected endogenous LIN54 and LIN9 (F).

(G) Protein structures of PCNA-PAF complex and RBBP4. PAF (blue) binds to PCNA (green) via R149-D156 AAs of PCNA (De Biasio et al., 2015) (upper panel). We located the putative PAF binding region in the extruded loop of the RBBP4 protein (D346-D361 AAs; dotted boxes) (lower panel). Each protein structure (PCNA-PAF: 6gws; RBBP4: 4pby) was modified from the Protein Data Bank in Europe (PDBe; http://www.ebi.ac.uk/pdbe/).

(H-J) Analysis of RBBP4-PAF interaction. (H) Protein sequence alignment of RBBP4 (UniProtKB - Q09028) and PCNA (UniProtKB - P12004). BLASTp analysis (https://blast.ncbi.nlm.nih.gov/Blast.cgi?PAGE=Proteins). (I) The PAF-binding region in PCNA is marked in pink. Protein structure of PCNA-PAF complex (PDBe: 6gws). Protein structure of RBBP4 (PDBe: 4pby). (J) The potential binding region for PAF in RBBP4's extruded region is marked in yellow. The amino acids in purple indicate the binding region for histone H4.

(K) Enrichment of DREAM components on target gene promoters in mouse LUAD cells. The promoter occupancy of p130, Rbbp4, and Lin54 on the representative DREAM complex target gene promoters (*Ccnb1*, *Top2a*, *Plk1*, and *Ube2c*) was analyzed by ChIP-qPCR in mouse (KP; control versus shPaf) cells. ChIP-qPCR.

(L) Enrichment of PAF with DREAM complex components on DREAM complex target gene promoters. PAF showed co-occupancy with RBBP4, LIN54, and BMYB in the DREAM target gene promoters (*CCNB1* and *PLK1*); Sequential ChIP-analysis. 1st ChIP for FLAG-PAF (anti-FLAG antibody) was followed by 2nd ChIP for the DREAM complex components (anti-p130, RBBP4, LIN54, and phosphor-BMYB antibodies). No-antibody condition and *ACTB* promoter were used as negative control; A549 cells.

(M and N) Interaction of PAF binding-deficient RBBP4 mutant with DREAM complex. (M) Co-IP results showed the interaction of RBBP4 mutants with p130 and LIN9. The Ctrl vector or PAF binding-deficient RBBP4 mutant (Δ347-362 AAs; FLAG-tagged at the N-terminus) was transiently expressed in A549 cells and subjected to co-IP assays for FLAG, followed by IB for p130 and LIN9. (N) The enrichment of the RBBP4 Δ347-362 mutant on DREAM complex target gene promoters; ChIP analysis.

(O) PAF mutPIP rescues the G0/G1 arrest induced by PAF depletion. The cell cycle phases were analyzed in A549 shPAF cells that stably expressed GFP (control), PAF mutPIP, or PAF mutPIP, mutRBM. PI staining with FACS analysis. Quantification of cell cycle phases shown in Figure 6P.

Representative images are shown; error bars: SEM; *$P < 0.05$; **$P < 0.01$.

Figure S7. Screening and Validation of Candidate Compounds Mimicking the PAF-Depleted Transcriptome, Related to Figure 7.

(A) Cell cycle analysis of mouse lung cancer cells (KP) treated with 11 drug candidates. KP cells were treated with each drug candidate (total n = 13, pitavastatin and CsA are shown in Figure 7C) for 24 h, followed by PI staining and FACS analysis. Chemicals that induced G0/G1 arrest (more than 5%; colored in red) compared to vehicle-treatment were selected for further analysis. PI staining and FACS (n = 20,000 cells).

(B) Gene expression analysis of DREAM target genes by qRT-PCR; KP cells were treated with each drug candidate for 48 h, followed by qRT-PCR analysis. $*P < 0.05$. Downregulation of DREAM target genes was prominently induced by pitavastatin (1 μM, 48 h) and by CsA (5 μM, 48 h).

(C and D) LUAD cell growth inhibition by pitavastatin or CsA in a dose-dependent manner. (C) Crystal violet staining images and (D) quantification of cell growth at each dose of pitavastatin or CsA treatment in human (H1792, H23, and A549) and mouse (KP836 and KP952) LUAD cells. OD values (OD_{590}) of crystal violet staining at the endpoint (3 to 6 days after treatment) were used to calculate GI_{50} (50% of growth inhibition) values (n = 3).

(E) Harmine treatment reduces the G0/G1 arrest induced by pitavastatin or CsA treatment. Quantification of the cell cycle distributions shown in Figures 7F and 7G; PI staining with FACS analysis.

(F) Pitavastatin or CsA treatment reduced PAF expression and proliferation in H1792 xenografts. Representative images of PAF and Ki67 immunostaining; endpoint tumors were used (n = 3). Quantification of Ki67-positive cells is presented in Figures 7J and 7L.

Representative images are shown; error bars: SEM; $*P < 0.05$; $**P < 0.01$.

Supplemental Figure 1

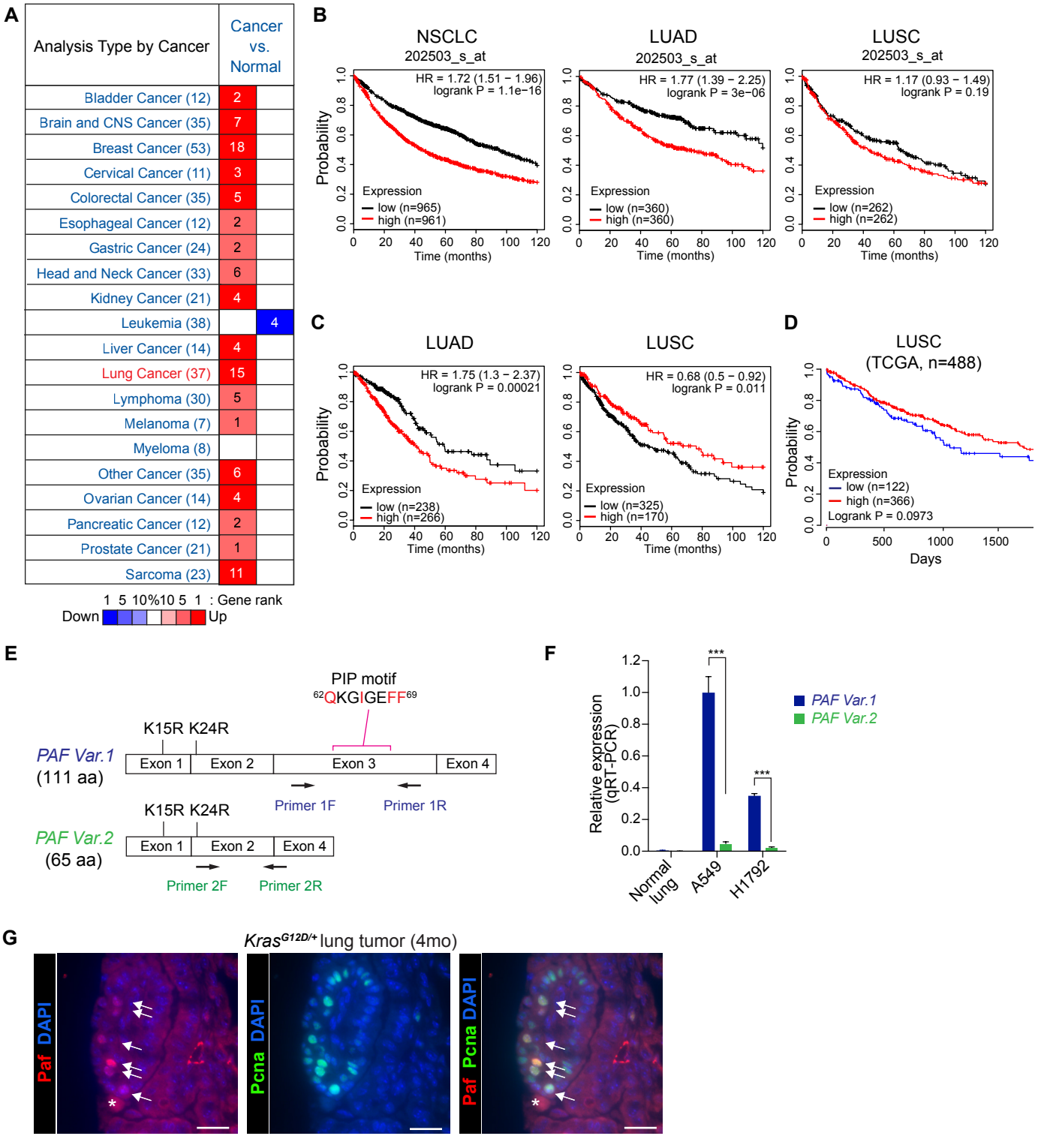

Supplemental Figure 2

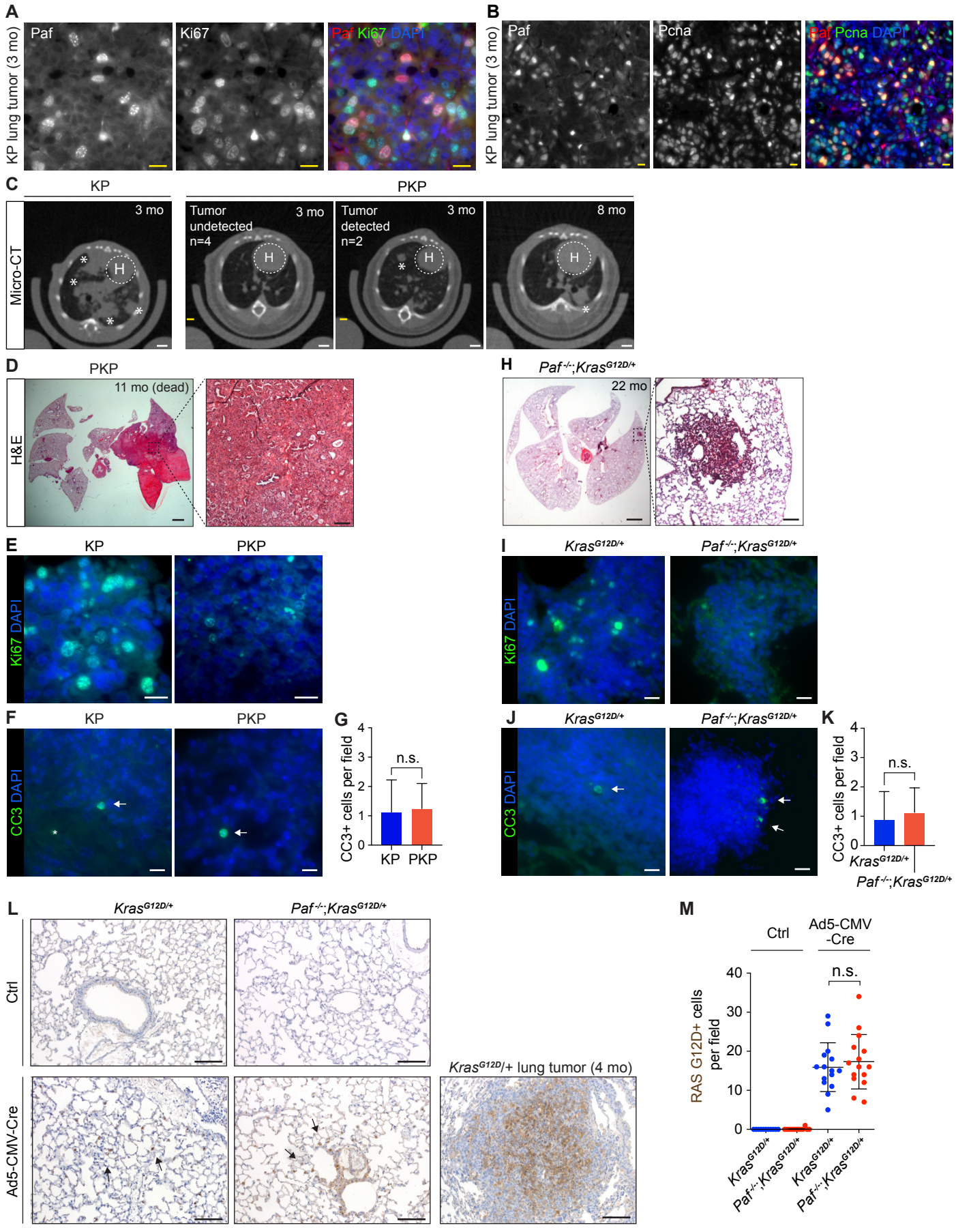

Supplemental Figure 3

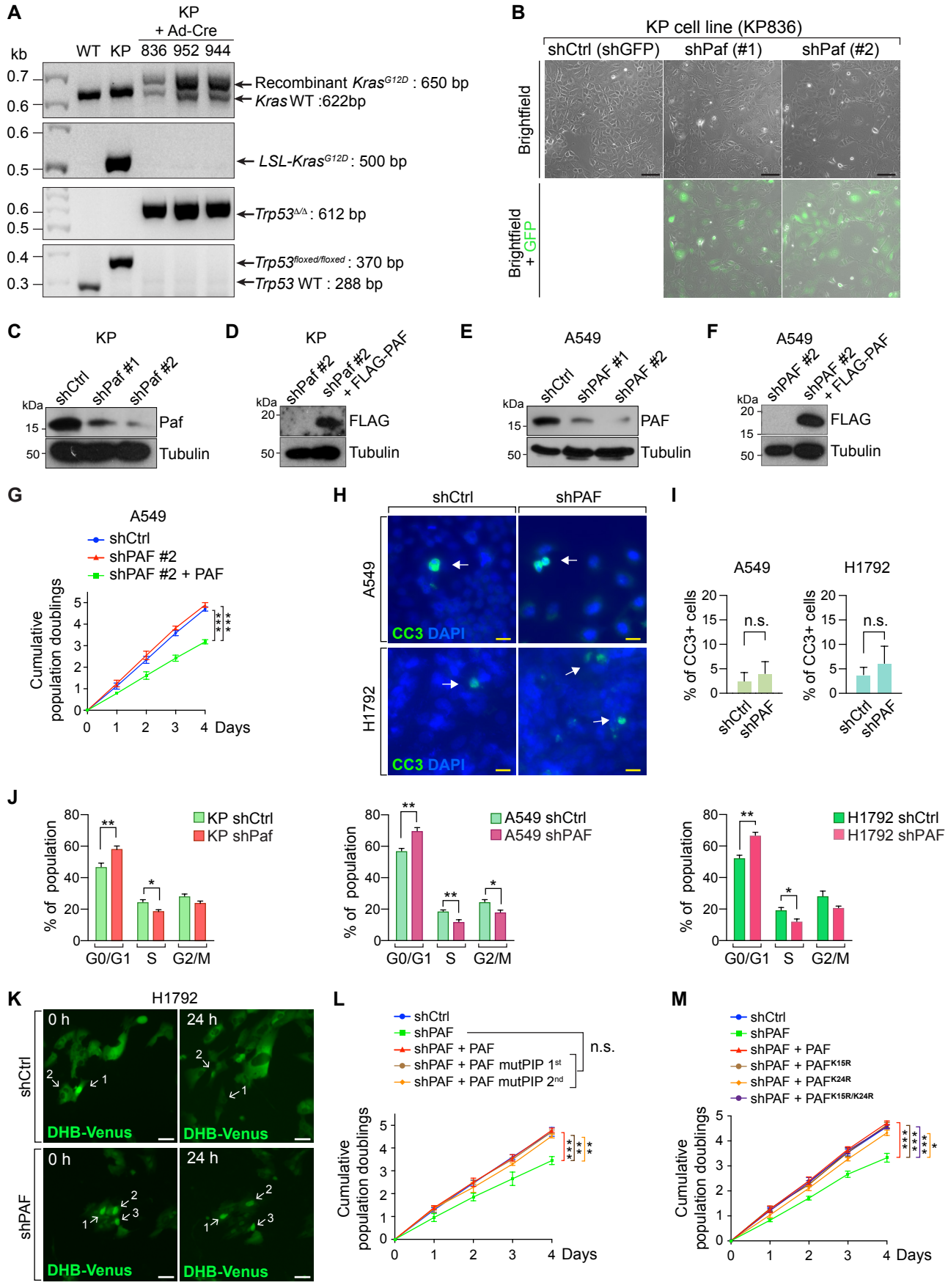

Supplemental Figure 4

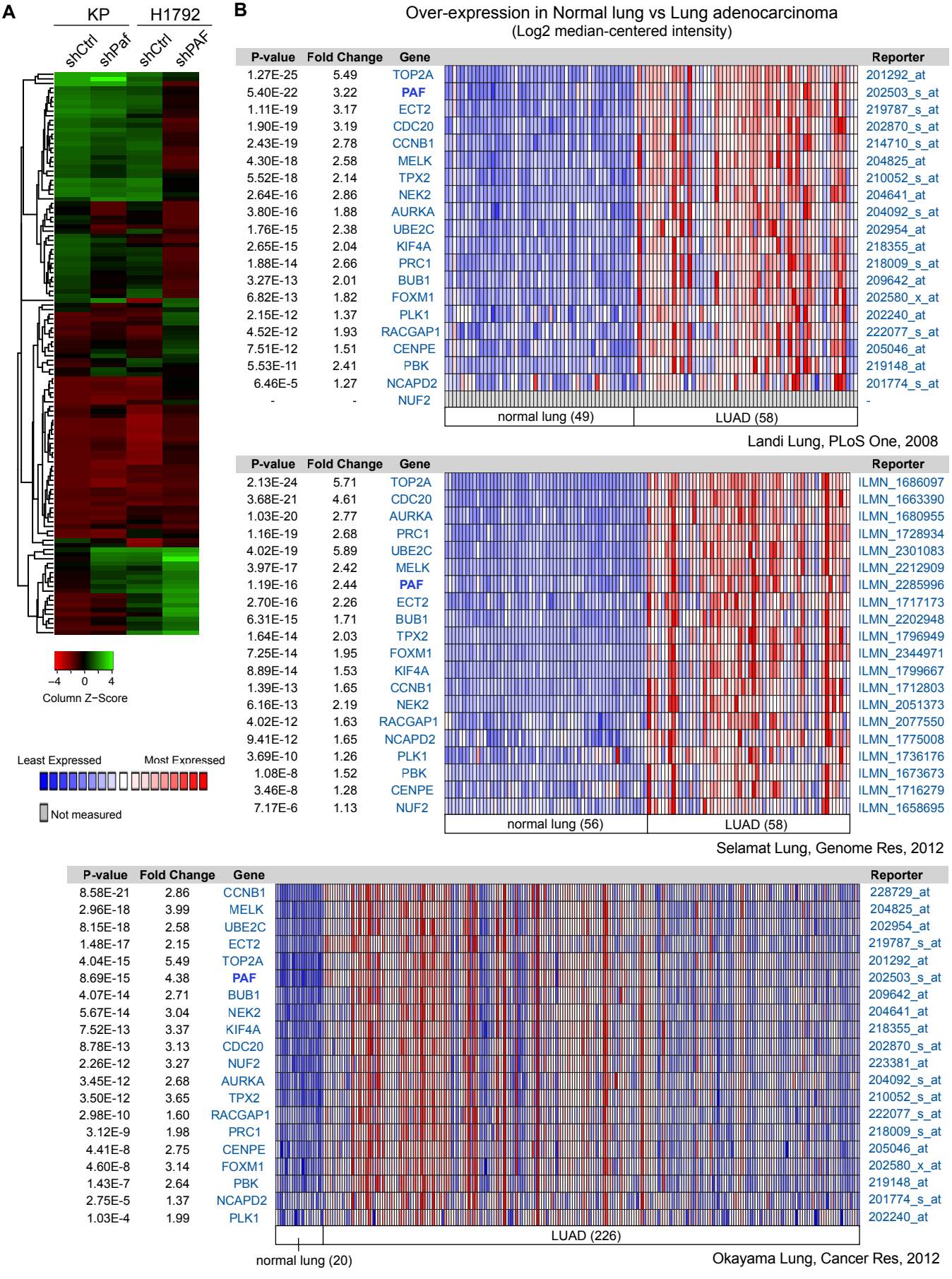

Supplemental Figure 5

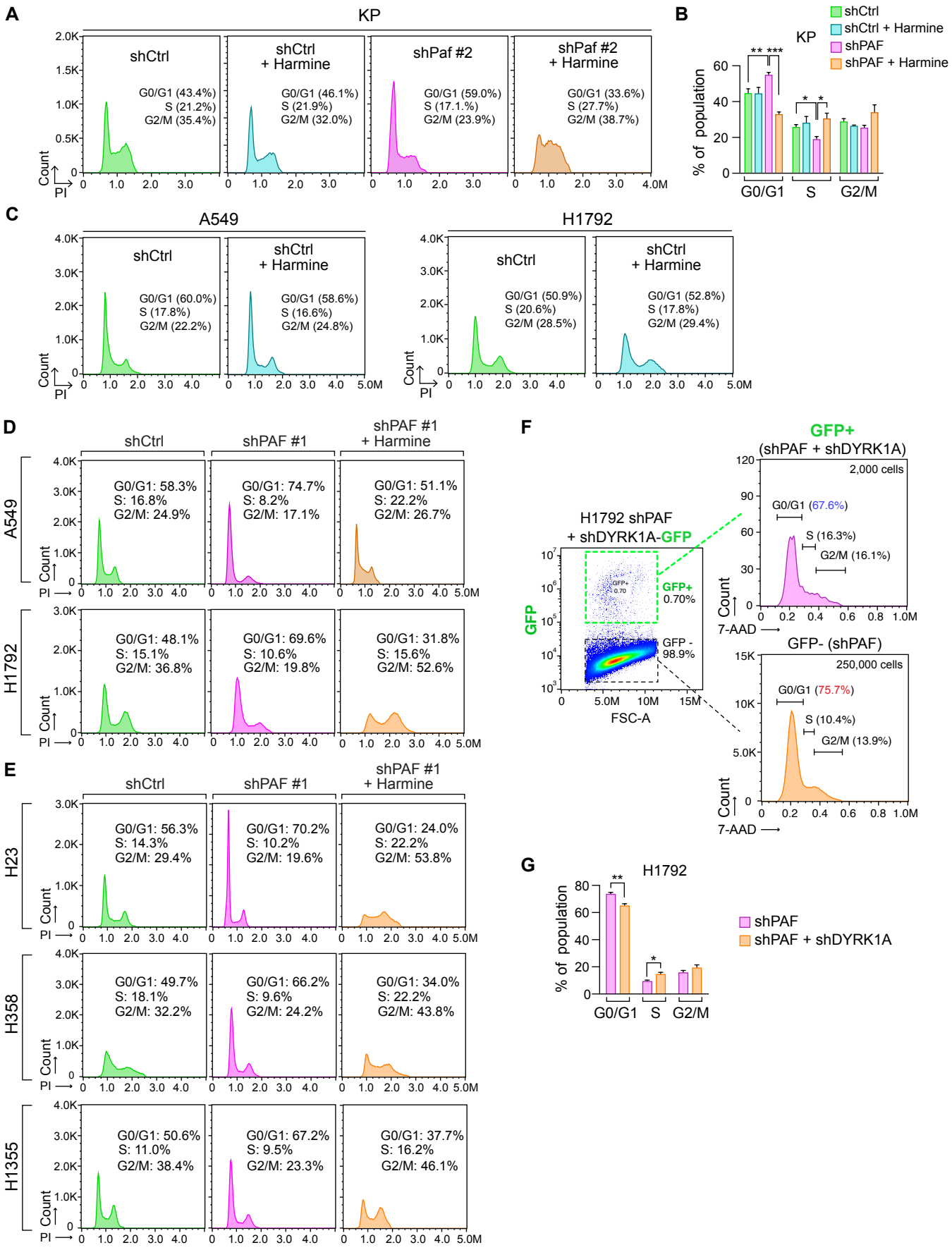

Supplemental Figure 6

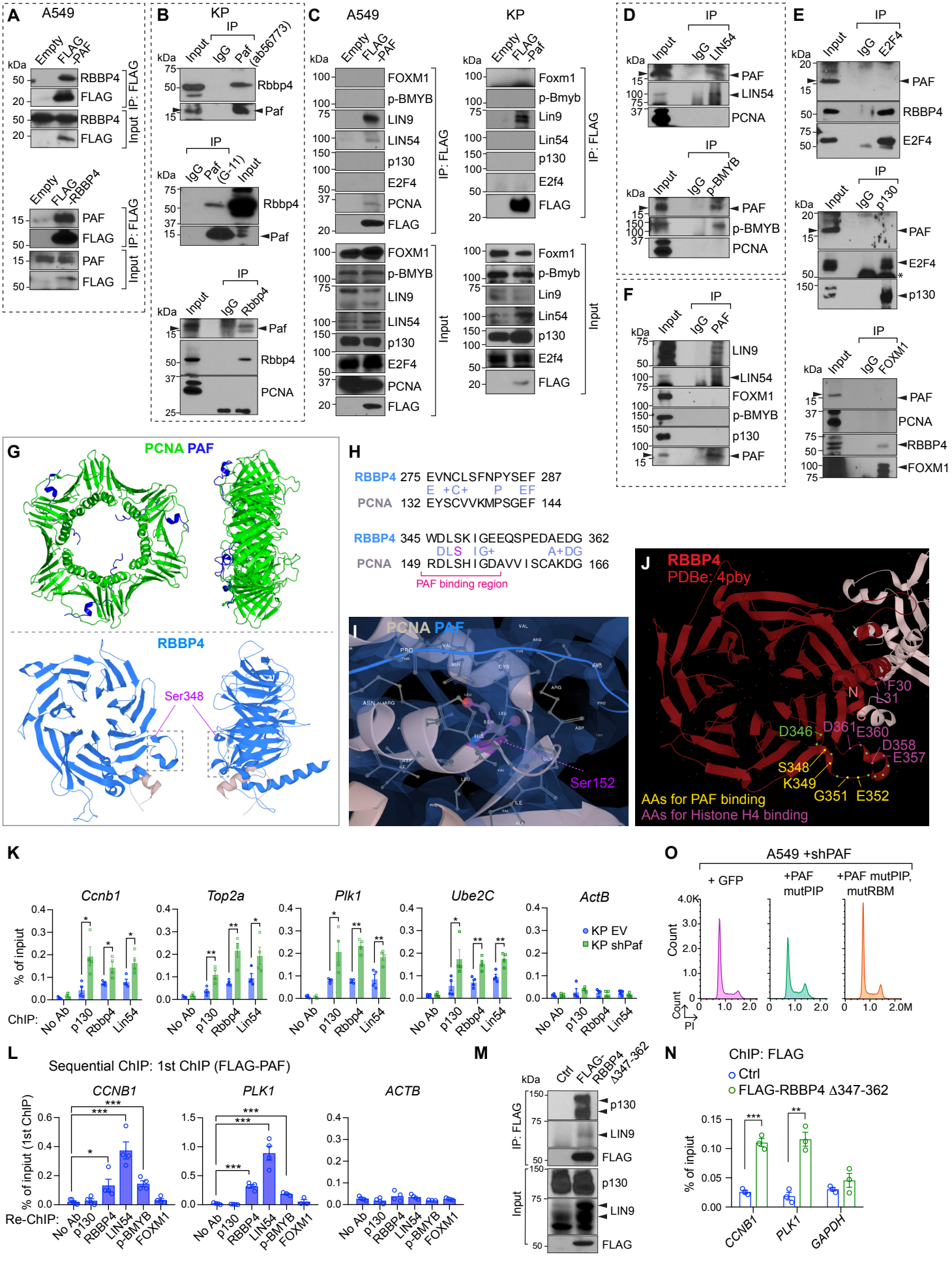

Supplemental Figure 7